https://ntrs.nasa.gov/search.jsp?R=20190026506 2020-05-06T09:49:14+00:00Z

Computational Analysis of the External Aerodynamics of the Unpowered X-57 Mod-III Aircraft

Seung Y. Yoo[1]
NASA Armstrong Flight Research Center, Edwards, California, 93523, USA

Jared C. Duensing[2]
Science & Technology Corporation, Moffet Field, California, 94035, USA

Investigations of the external aerodynamics of the unpowered X-57 Mod-III configuration using computational fluid dynamics are presented. Two different Reynolds-averaged Navier-Stokes flow solvers were used in the analysis: the STAR-CCM+ unstructured solver using polyhedral grid topology, and the Launch Ascent Vehicle Aerodynamics (LAVA) structured curvilinear flow solver using structured overset grid topology. A grid refinement study was conducted and suitable grid resolution was determined by examining the forces and moments of the aircraft. Code-to-code comparison shows that STAR-CCM+ and LAVA are in good agreement both in quantitative values and trends. The angle-of-attack sweep and sideslip-angle sweep were performed. Results indicate that lift coefficients have a sharp drop at stall. At high angle of attack, STAR-CCM+ and LAVA show different flow separation behavior possibly due to differences in the turbulence model. The sideslip-angle sweep results show constant pitching moment from 0° to 15°, then a sharp increase between 15° and 20° sideslip angle.

I. Nomenclature

AFRC	=	Armstrong Flight Research Center
ARC	=	Ames Research Center
C_D	=	drag coefficient
C_L	=	lift coefficient
C_Y	=	side-force coefficient
C_l	=	rolling-moment coefficient
C_m	=	pitching-moment coefficient
C_n	=	yawing-moment coefficient
CAD	=	computer-aided design
CFD	=	computational fluid dynamics
LAVA	=	Launch Ascent Vehicle Aerodynamics
NASA	=	National Aeronautics and Space Administration
RANS	=	Reynolds-averaged Navier-Stokes
y+	=	non-dimensional wall distance

II. Introduction

The X-57 Maxwell, or Scalable Convergent Electric Propulsion Technology and Operations Research (SCEPTOR), is one of the X-planes funded by Flight Demonstration and Capabilities (FDC) under the Integrated

[1] Aerospace Engineer, Controls and Dynamics, P.O. Box 273, MS 4840D, Edwards, California, 93523-0273.
[2] Computational Aerosciences Branch, NAS Division, Moffett Field, California, 94035.

Aviation Systems Program (IASP) in the Aeronautics Research Mission Directorate (ARMD) of the National Aeronautics and Space Administration (NASA). The X-57 program has several key research objectives aimed at reducing aviation energy usage. The research objectives include demonstration of a propeller-based distributed electric propulsion (DEP) system, reduction of induced drag through wing-tip-mounted propellers, and improved lift efficiency using leading-edge high-lift motors and nacelles.

The X-57 program is divided into several phases, denoted by the modification (Mod) made to the airplane. Each Mod modifies the existing TECNAM P-2006T aircraft (Costruzioni Aeronautiche TECNAM S.p.A, Capua, Italy) in a systematic and modular manner to achieve each research objective. There are four Mods, as shown in Fig. 1. The Mod-I, shown in Fig. 1(a), is the original TECNAM P-2006T aircraft, which serves as the baseline for the performance comparison. The Mod-II, shown in Fig. 1(b), replaces the original engine and propellers with an electrical propulsion system and optimized propellers. The Mod-III, shown in Fig. 1(c), replaces the wing of Mod-II with a high-aspect-ratio wing with and wing-tip-mounted propellers. The wing-tip propellers rotate in the direction that counteracts the wing-tip vortices, intended to reduce induced drag. The Mod-IV, shown in Fig. 1(d), incorporates the leading-edge-mounted high-lift propellers to Mod-III to provide additional lift at takeoff and landing conditions.

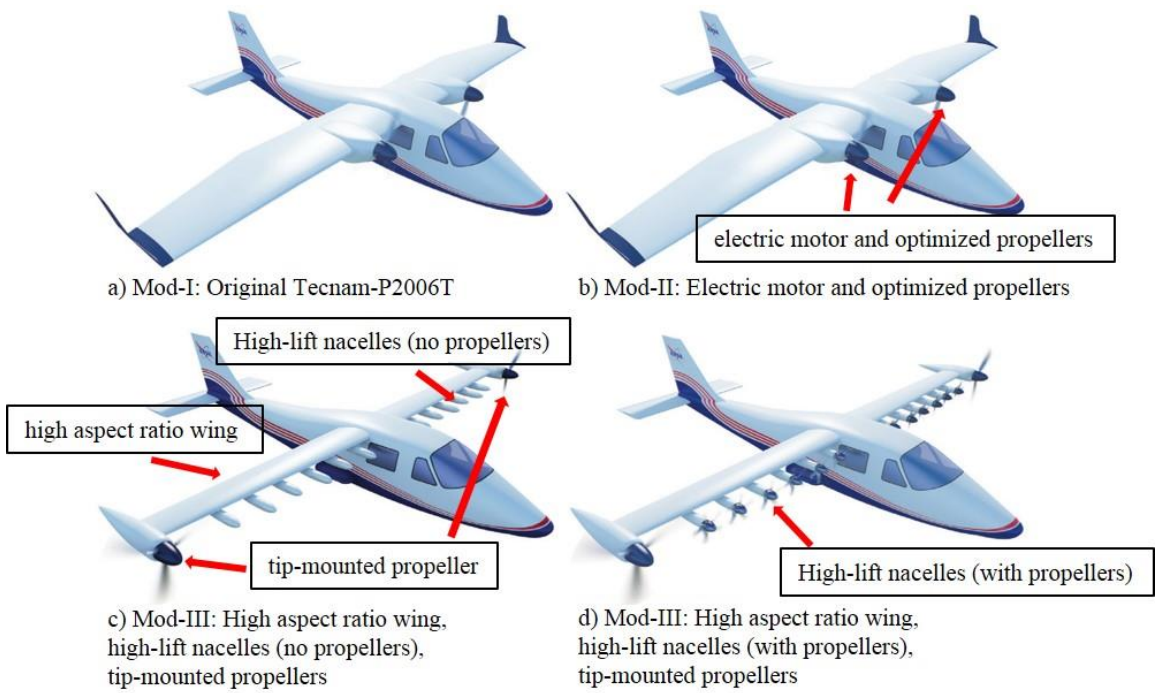

a) Mod-I: Original Tecnam-P2006T

b) Mod-II: Electric motor and optimized propellers

c) Mod-III: High aspect ratio wing, high-lift nacelles (no propellers), tip-mounted propellers

d) Mod-III: High aspect ratio wing, high-lift nacelles (with propellers), tip-mounted propellers

Fig. 1. X-57 modification (Mod) comparison.

As the X-57 is a manned experimental project, a significant amount of precaution is taken prior to the flight-test campaign. The safety of the pilot and the aircraft are of the highest priority, thus the external flow physics of the aircraft are investigated and examined using computational fluid dynamics (CFD) simulations and analysis techniques. Due to limited wind tunnel testing, the CFD results are used in conjunction with wind-tunnel experimental data to develop the aerodynamics database that is used in the pilot-in-the-loop simulation. The pilot-in-the-loop simulation is used for aircraft familiarization trainings and for the mission.

This paper presents the results of the CFD analysis that was performed, specifically angle-of-attack sweeps and sideslip-angle sweeps, on the unpowered X-57 Mod-III configuration. The angle-of-attack sweeps and sideslip-angle sweeps were performed for three different flap-deflection angles: cruise (0.0°); takeoff (10.0°); and landing (30.0°). The works presented are predecessors of the powered X-57 Mod-III and Mod-IV analysis as well as aerodynamic database generation. The term “aircraft” is used herein to describe the unpowered X-57 Mod-III.

The NASA Armstrong Flight Research Center (AFRC) and the NASA Ames Research Center (ARC) collaborated in the effort. The AFRC used a commercially available STAR-CCM+ [1] unstructured solver while ARC used the in-house-developed Launch Ascent Vehicle Aerodynamics (LAVA) structured curvilinear solver [2].Simulation settings and modeling techniques were based on previous work that developed the best practices for simulating the X-57 wind-tunnel model using the same solvers [3].

Section II below describes the flow solvers and the numerical settings utilized in the investigation. Section III presents the geometry and grid generation process. Section IV presents results and associated discussions. Section V summarizes the findings.

III. Flow Solvers

This section presents the solvers and the numerical settings used to perform the simulations. Two different Reynolds-averaged Navier-Stokes (RANS) equation solvers were used to analyze the aircraft: the STAR-CCM+ unstructured solver, and the LAVA structured curvilinear solver.

A. STAR-CCM+

The STAR-CCM+ is a commercially available CFD package that includes geometry / computer-aided design (CAD) manipulation tools, a grid generator capable generating different unstructured grid topologies (polyhedral, Cartesian, tetrahedral), various flow solvers, and post-processing tools. The flow solvers of STAR-CCM+ solve the RANS equation in finite-volume, cell-centered formulation. The compressible flow solver using the steady-state, implicit time-stepping scheme was utilized. The inviscid fluxes were discretized using the second-order Roe flux-difference splitting scheme. The algebraic multigrid linear solver using the Gauss-Seidel relaxation scheme was employed to solve the system of linearized equations. The gradients were computed using the hybrid Gauss least-squares method and limited using the Venkatakrishanan scheme [4]. A low-Mach preconditioner was not utilized so as to be consistent with LAVA solver settings. The flow was assumed fully turbulent and the Spalart-Allmaras turbulence model with the rotational correction was used to resolve the turbulence [5]. The quadratic constitutive relationship [6] was not utilized due to lack of availability in STAR-CCM+ for the Spalart-Allamaras model. The Courant-Friedrichs-Lewy (CFL) number was linearly ramped from 0.01 to 25.0 in the initial 100 iterations. All simulations were performed using the freestream condition as the initial solution.

B. Launch Ascent Vehicle Aerodynamic (LAVA)

LAVA was developed and it is maintained by ARC. Similar to STAR-CCM+, it consists of several different flow solvers and it is capable of using various grid topology (Cartesian, unstructured polyhedral, structured overset) depending on the choice of the solver. The structured curvilinear solver was used in this study. A second-order convective flux discretization with first-order upwind scheme in time was used with a Van-Albada slope limiter. Fully turbulent flow was assumed and the Spalart-Allmaras turbulence model [5] was used with the quadratic constitutive relation [6] and rotation correction. As with STAR-CCM+, the low Mach preconditioner was not utilized. All simulations were performed using the freestream condition as the initial solution. More detail can be found in the previous study [3].

IV. Geometry and Grid Generation

This section presents the detail of the geometry and grid generation process. The 100 percent scale model of the X-57 Mod-III configuration was used to perform the simulations. All control surfaces (ailerons, rudder, stabilator, and trim tab) and their deflections were modeled. Three nominal flap-deflection angles were modeled: 0° deflection (cruise); 10° deflection (takeoff); and 30° deflection (landing). The flap deflections are listed in Table 1.

Table 1. Flap-deflection angles and associated flight phase.

Flight phase	Flap-deflection angle, deg
Cruise	0
Takeoff	10
Landing	30

Important dimensions and reference parameters of the aircraft such as the mean the aerodynamic chord, span, and wing area are tabulated in Table 2. The origin of the main coordinate system with respect to the nose leading edge of the aircraft and the moment reference center with respect of the origin of the main coordinate system are also tabulated in Table 2. The main coordinate system is defined with the x-axis pointing in the direction from the nose to tail of the aircraft, the y-axis in the direction out the right wing, and the z-axis pointing up based on the right-hand coordinate system. The body-axis coordinate system, with its origin at the moment reference center, is defined with the x-axis in the direction from tail to the nose of the aircraft, the y-axis in the direction out the right wing, and the z-axis pointing down based on the right-hand coordinate system. Figure 2 shows the main coordinate system and the body-axis

coordinate system. The positive control surface deflections, defined based on the trailing edge orientation, are tabulated in Table 3.

Table 2. The X-57 geometric parameters used in the study.

Parameter	Value
Mean aerodynamic chord	2.13 ft
Span	31.633 ft
Wing area	66.667 ft^2
Moment reference center with respect to origin	(12.8997, 0.0, 5.377) ft
Origin with respect to nose	(-1.889, 0.0, 4.242) ft

Table 3. Positive control surface deflection orientation.

Control surface	Positive deflection
Aileron	Trailing edge down
Rudder	Trailing edge left
Stabilator	Trailing edge down
Pitch trim tab	Trailing edge down

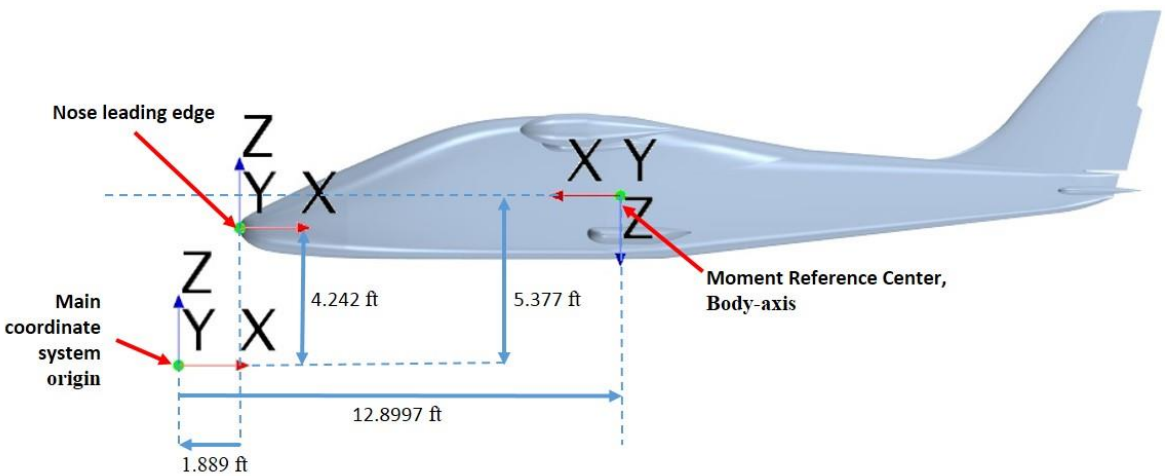

Fig. 2. Coordinate system orientations and origins.

Using the identical underlying model, computational grids were generated independently for STAR-CCM+ and LAVA as the two solvers utilize different types of topology: STAR-CCM+ used the unstructured polyhedral grid topology while LAVA used the structured overset grid topology. The following subsections describe the grid generation process and settings. The terminologies “grid” and “mesh” are used interchangeably herein.

A. Grid Generation with STAR-CCM+

As a comprehensive CFD package, STAR-CCM+ contains its own geometry manipulation and grid generation tools which were utilized in this work. Individual control surfaces (aileron, rudder, stabilator, and pitch trim tab) were modeled such that they can be deflected independently. The flap deflections were modeled in the CAD model, and thus were not manipulated within the STAR-CCM+ environment.

Grids based on the STAR-CCM+ polyhedral grid topology combined with the prism layer grid were created using the STAR-CCM+ grid generator. Half of the aircraft was modeled utilizing the symmetry boundary condition unless asymmetric geometry (aileron or rudder deflection) or flow condition (nonzero sideslip condition) was present. Essential grid parameters such as the growth ratio, cell size, far field length, et cetera were specified based on the gridding guidelines provided by the American Institute of Aeronautics and Astronautics (AIAA) CFD High Lift Prediction Workshop [7] as well as best practices developed during previous work [3]. The prism layer grid of 31 layers was created to capture the flow in the boundary layer. The total height of the prism layer was initially specified based on the turbulent boundary layer thickness, then adjusted based on the results of background studies.

Grid wall spacing was determined based on the wing y+ value of 0.3. The far field distance was specified as a 50 wing-span length. The surface cell size of individual components of the aircraft (fuselage, vertical tail, rudder, stabilator, and wing) were specified as a percentage of a grid reference length to simplify the process of systematically creating grids of different resolution. A representative polyhedral surface grid of the aircraft is shown in Fig. 3.

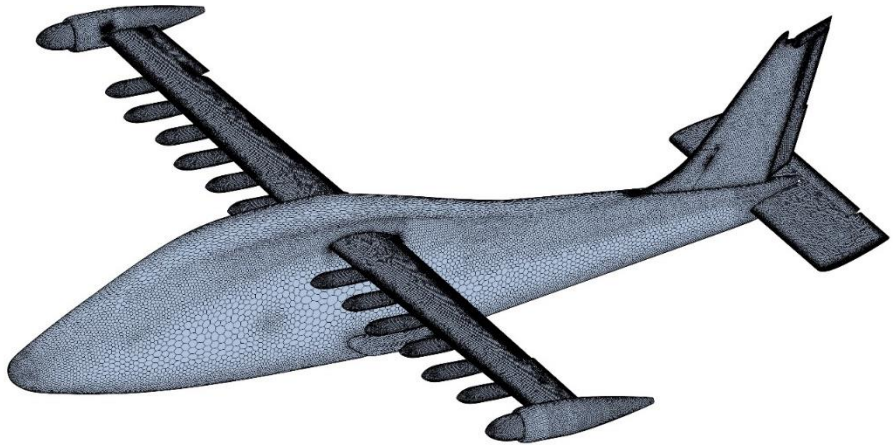

Fig. 3. Representative STAR-CCM+ polyhedral surface grid of the X-57 with all control surfaces deflected to maximum deflection angle.

B. Grid Generation with Lauch Ascent Vehicle Aerodynamics (LAVA)

Structured overset grids were created to model the X-57 Mod-III configuration. Various tools were utilized in the grid generation process. The ANSA [8], a CAD and mesh generation software, was used to discretize the provided model which served as the basis for the overset grids. The Pointwise grid generation software [9] (Pointwise, Inc., Fort Worth, Texas) and Chimera Grid Tools [10] were used to create the structured overset grids. As with the models used in STAR-CCM+ simulations, all of the control surfaces were modeled independently. A full span model was utilized regardless of the symmetry. The initial volume grid spacing was based on the wing y+ value of 1.0 or smaller, depending on the grid resolution level. The nearfield grids were generated using the curvilinear grids and the farfield grids were created using the Cartesian grids. An in-house-developed grid connectivity tool was applied to the volume grids to interpolate the overlapping grids. The surface grids are shown in Fig. 4. Full details of the control-surface modeling and grid generation parameters are presented in a previously published study [3].

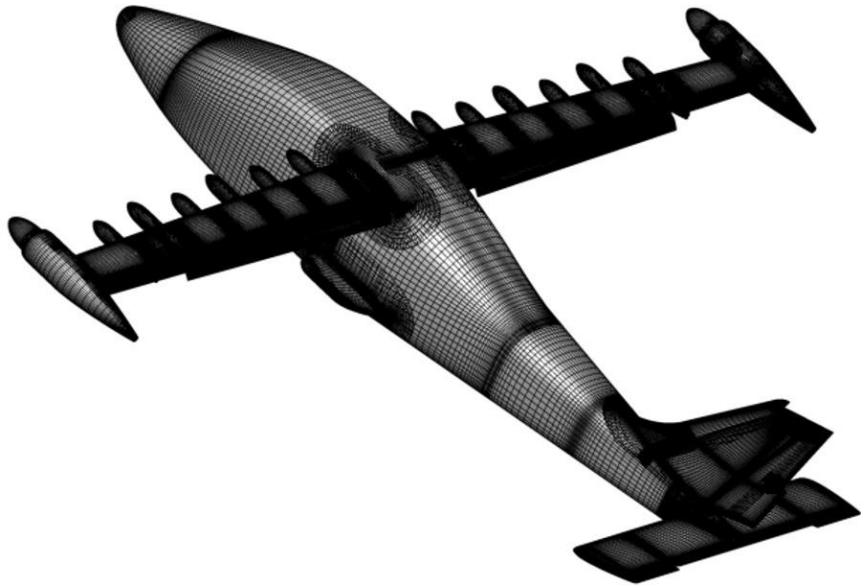

Fig. 4. Representative structured overset surface grids used with Launch Ascent Vehicle Aerodynamics (LAVA).

V. Results

Computational fluid dynamics simulation results are presented in this section. The force and moment coefficients are presented for all simulations performed. The lift coefficient (C_L), drag coefficient (C_D), and side-force coefficient (C_Y) were normalized using the wing area. The rolling-moment coefficient (C_l) and yawing-moment coefficient (C_n) were normalized using the wingspan and wing area. The pitching-moment coefficient (C_m) was normalized using the mean aerodynamic chord and wing area. The moment coefficients were computed about the moment reference center provided in Table 2. The C_D and C_L were computed about the stability axis and the C_Y, C_l, C_m, and C_n were computed about the body axis coordinate system. The origin of the stability axis and the body axis were placed at the moment reference center.

The results are presented in the following order. First, the results of the grid refinement study are presented which determined the grid resolution necessary to resolve the flow physics. Succeeding the grid refinement study, the angle-of-attack sweep study and the sideslip-angle sweep study are presented.

The angle-of-attack sweeps and sideslip-angle sweeps were conducted for three different flap-deflection angles as tabulated in Table 1: 0° deflection (cruise), 10° deflection (takeoff), and 30° deflection (landing) with the respective atmospheric conditions associated with each flap-deflection angle. The atmospheric conditions per flap-deflection angles are tabulated in Table 4. The angles of attack and sideslip angles simulated for each flap deflection are tabulated in Table 5.

All figures presented in the following subsections identify the STAR-CCM+ results with blue color and the LAVA results with red color. All line plots presented show the 0° flap-deflection results with solid lines, the 10° flap-deflection results with dashed lines, and the 30° flap-deflection results with dash-dot lines.

Table 4. Atmospheric conditions for flap deflections.

	Flap = 0°	Flap = 10°	Flap = 30°
Altitude, ft	8000	2500	2500
Mach	0.233	0.149	0.139
Density, slug/ft^3	1.8628E-3	2.20782E-3	2.20782E-3
Static pressure, lbf/ft^2	1571.9	1931.9	1931.9
Static temperature, K	272.3	283.2	283.2
Coefficient of viscosity, slug/ft/s	3.57532E-7	3.68708E-7	3.68708E-7
Reynolds number	1.32E6	9.875E5	9.21E5

Table 5. Angle-of-attack sweep and sideslip-angle sweep run matrix.

	Flap deflection, deg	Angle of attack, deg	Sideslip angle, deg
Angle-of-attack sweep	0	-2, 0, 2, 4, 8, 10, 12, 14, 15, 16, 17, 18, 19, 20, 22, 24	0
	10	-2, 2, 4, 8, 10, 12, 13, 14, 15, 16, 18, 20, 22	0
	30	-2, 2, 4, 8, 9, 10, 11, 12, 13, 14, 15, 16, 17, 18, 20, 24	0
Sideslip-angle sweep	0	2	0, 5, 10 (STAR-CCM+ only), 15 (STAR-CCM+ only)
	10	2	0, 5, 10 (STAR-CCM+ only), 15 (STAR-CCM+ only)
	30	2	0, 5, 10 (STAR-CCM+ only), 15 (STAR-CCM+ only)

A. Grid Refinement Study

A grid refinement study was performed to determine the grid resolution requirement needed to resolve flow phenemona. The aircraft configuration of maximum control surface deflections, largest angle of attack, and largest sideslip angle was used in the study. The freestream flow angles and control surface deflection angles are tabulated in Table 6. The atmospheric condition used is tabulated in Table 7.

Three different grid resolutions were simulated using STAR-CCM+: a coarse grid of 45 million cells, a medium grid of 77 million cells, and a fine grid of 126 million cells. The force and moment coefficients for each grid resolution are tabulated in Table 8. The relative errors of coarse and medium grid with respect to the fine grid are tabulated in Table 9. Results showed that, with the exception of C_l, the relative error of the force and moment coefficients of both the coarse and the medium grid are under 3 percent with respect to the fine grid. The coarse grid underestimates the C_l by 17.7 percent relative to the fine grid, whereas the medium grid over-predicts C_l by 1.1 percent. The values of C_l are, however, small - close to zero - which is prone to large relative error. Based on the result presented, the coarse grid was selected to perform the STAR-CCM+ CFD simulations, identified in the tables using bold text.

For LAVA, five different grid resolutions were simulated: a coarse grid of 60.1 million nodes, a medium grid of 95.2 million nodes, a fine grid of 148.6 million nodes, a very-fine grid of 312.6 million nodes, and an extra-fine grid of 425.7 million nodes. The force and moment coefficients and their respective relative error to the extra-fine grid are presented in Table 10 and Table 11, respectively. Similar to STAR-CCM+ results, relative errors are small as they are under 4 percent except for C_l. The relative errors of the rolling moment coefficient are, however, converging toward the extra-fine grid, and the absolute value of the coefficient is small and susceptible to large relative error. Based on the results, the fine grid was selected to perform the LAVA CFD simulations, identified in the tables using bold text.

Using the LAVA results as the reference, the STAR-CCM+ results are within 10 percent of the LAVA results for the force and moments coefficients. The coefficient with the largest difference is C_l, with STAR-CCM+ underestimating it by 9.9 percent relative to the LAVA solution. The C_D has the smallest relative difference, with STAR-CCM+ overestimating it by 1.2 percent relative to LAVA. The force and moment coefficient of the selected grid resolution for the STAR-CCM+ and LAVA are summarized in Table 12.

Table 6. Aircraft orientation and control-surface-deflection used in grid refinement study.

Parameter	Angle, deg
Angle of attack	10
Sideslip angle	20
Aileron	-25
Flap	30
Rudder	-28
Stabilator	-15
Trim tab	-18

Table 7. Atmospheric conditions used in grid refinement study.

Altitude, ft	2500
Mach	0.139
Density, slug/ft^3	2.20782E-3
Static pressure, lbf/ft^2	1931.9
Static temperature, K	283.2
Coeffficient of viscosity, slug/ft/s	3.68708E-7
Velocity, ft/s	153.87
Reynolds number	9.21E5

Table 8. STAR-CCM+ forces and moments for grid refinement study for full deflection; selected resolution shown in bold.

STAR-CCM+ grid resolution	C_D	C_L	C_Y	C_l	C_m	C_n
coarse (45e6 cells)	**0.30394**	**1.46749**	**-0.61327**	**0.01631**	**2.41895**	**0.12050**
medium (77e6 cells)	0.30623	1.47778	-0.61585	0.02004	2.41327	0.12257
fine (126e6 cells)	0.30797	1.47193	-0.61886	0.01982	2.38941	0.12337

Table 9. STAR-CCM+ force and moment coefficient error with respect to fine grid; selected resolution shown in bold.

STAR-CCM+ grid resolution	C_D error, %	C_L error, %	C_Y error, %	C_l error, %	C_m error, %	C_n error, %
coarse (45 mil. cell)	**-1.1**	**-0.3**	**-0.9**	**-17.7**	**1.2**	**-2.3**
medium (77 mil. cell)	-0.5	0.4	-0.5	1.1	1.0	-0.6

Table 10. LAVA forces and moments for grid refinement study for full deflection; selected resolution shown in bold.

LAVA grid resolution	C_D	C_L	C_Y	C_l	C_m	C_n
coarse (60.1 mil. nodes)	0.3024	1.57	-0.6053	0.0135	2.396	0.1119
medium (95.2 mil. nodes)	0.29838	1.55	-0.595	0.016	2.404	0.1117
fine (248.6 mil. nodes)	**0.30036**	**1.56**	**-0.5876**	**0.0181**	**2.398**	**0.1106**
very-fine (312.6 mil. nodes)	0.30265	1.56	-0.5844	0.0226	2.402	0.1121
extra-fine (425.7 mil nodes)	0.30237	1.56	-0.582	0.0239	2.401	0.1126

Table 11. LAVA force and moment coefficient error with respect to X-fine grid; selected resolution shown in bold.

LAVA grid resolution	C_D error, %	C_L error, %	C_Y error, %	C_l error, %	C_m error, %	C_n error, %
coarse (60.1 mil. nodes)	-0.01	-0.64	-4.00	43.51	0.21	0.62
medium (95.2 mil. nodes)	1.32	0.51	-2.23	33.05	-0.12	0.80
fine (248.6 mil. nodes)	**0.66**	**-0.26**	**-0.96**	**24.27**	**0.12**	**1.78**
very-fine (312.6 mil. nodes)	-0.09	-0.32	-0.41	5.44	-0.04	0.44

Table 12. STAR-CCM+ and LAVA force and moment coefficients of selected grid resolution; selected resolution shown in bold.

Flow solver	C_D	C_L	C_Y	C_l	C_m	C_n
LAVA	0.30036	1.56	-0.5876	0.0181	2.398	0.1106
STAR-CCM+	0.30394	1.47	-0.6133	0.0163	2.419	0.1205

B. Angle-of-Attack Sweep

Results of the angle-of-attack sweep for three flap deflections, shown in Table 1, are presented in this section. Control surfaces other than the flap were set to the neutral position (no deflection). The atmospheric conditions for each flap deflection are tabulated in Table 4. The following discussions analyze flow physics as well as the differences in solutions of the two solvers.

The results of C_L, presented in Fig. 5, show that STARCCM+ and LAVA results compare well for the angles of attack in the linear lift curve slope region for all three flap deflections. Results also show, however, that there is increase in difference in C_L between STAR-CCM+ and LAVA with an increase in flap-deflection angle in the linear lift curve slope region. This trend can be analyzed using the surface pressure coefficient contours and streamline on the upper surface of the wing at 8° angle of attack for 0°, 10°, and 30° flap deflection, shown in Fig. 6. Blue arrows in the figure point to locations on the wing having different flow feature between two solvers. At 0° flap deflection, shown in Fig 6(a), STAR-CCM+ and LAVA both show similar solution of attached flow. At 10° flap deflection, shown in Fig. 6(b), STAR-CCM+ shows a small separation region on the outboard trailing edge of the wing that is not present in the LAVA solution. At 30° flap deflection, shown in Fig. 6(c), the STAR-CCM+ result shows a clearly separated region on the outboard trailing edge of the wing, while the LAVA result shows attached flow. Thus the STAR-CCM+ estimates a lower C_L.

Comparing the C_L at higher angle of attack, near stall, the discrepancies in solution produced by STAR-CCM+ and LAVA are large due to differences in the separation behavior predicted by the two solvers. An example is shown in the surface pressure coefficient contour of the wing for the 30° flap-deflection angle, presented in Fig. 7. Blue arrows point to locations on the wing having a different flow feature between two solvers. The surface pressure contour

at 8° angle of attack, shown in Fig 7(a), shows the STAR-CCM+ result with a thin separation region in the outboard trailing edge, as discussed above. At 14° angle of attack, shown in Fig 7(b), the STAR-CCM+ result shows flow separation in the wing root region that is not present in the LAVA solution. The results of both solvers show separation at the outboard of the wing at 14° angle of attack. At 18° angle of attack, shown in Fig 7(c), the STAR-CCM+ solution shows three separated regions while the lAVA solution shows the two separated regions. The differences in the flow separation are reflected in the C_L curve: STARCCM+ predicts a lower C_L in the post-stall angle of attack compared to LAVA. The cause of the difference is possibly due to the quadratic constitutive relation that is used in LAVA but is not used in STAR-CCM+, shown to affect the wing-fuselage junction flow [6].

Examining the C_L at the stall for all three flap deflections, shown in Fig. 5, the drop in C_L at the stall is not significant. The 0° flap deflection, shown with notation in Fig. 8, is used as an example. The LAVA result shows an 11.7-percent drop relative to the maximum C_L between the angle of attack of 19° (angle of attack of maximum C_L) and that of 22°. The STAR-CCM+ result shows a larger but more gradual drop in lift compared to LAVA: an 18.3-percent drop relative to the maximum C_L between the angle of attack of 17° (angle of attack of maximum C_L) and that of 22°. To provide a basis of comparison, the STAR-CCM+ CFD analysis of the NASA Gulfstream GIII (Gulfstream Aerospace Corporation, Savannah, Georgia) aircraft showed a 27.5-percent sharp drop in lift at stall relative to maximum lift [11].

The C_D compare well at low angles of attack for all three flap deflections, as shown in Fig. 9. The STAR-CCM+ predicts a higher C_D at 15°, 16°, and 17° angles of attack for 0°, 10°, and 30° flap deflection, respectively. The C_m, presented in Fig. 10, shows that STAR-CCM+ and LAVA compare well. Examining the C_m of the 0° flap deflection, shown in Fig. 10, there can be seen a sudden increase in C_m at angles of attack above 20° that is not shown in other flap deflections. For clarity, C_m as a function of angle of attack for 0° flap deflection is shown in Fig. 11. This phenomena can be correlated to the surface pressure coefficient contour of the aircraft at 22° angle attack for 0° and 10° flap deflection, shown in Fig. 12. A large separation bubble that envelops the majority of the upper surface exists on the stabilator at 0° flap deflection, shown in Fig. 12(a). On the 10° flap deflection configuration, shown in Fig. 12(b), the stabilator has a separation region that is localized to the inboard of the upper surface and grows from the leading edge to trailing edge. Based on the size of the separation region shown, the stabilator of 10° flap-deflection configuration would produce more lift compared to that of the 0° flap-deflection configuration, hence producing more nose-down pitching moment.

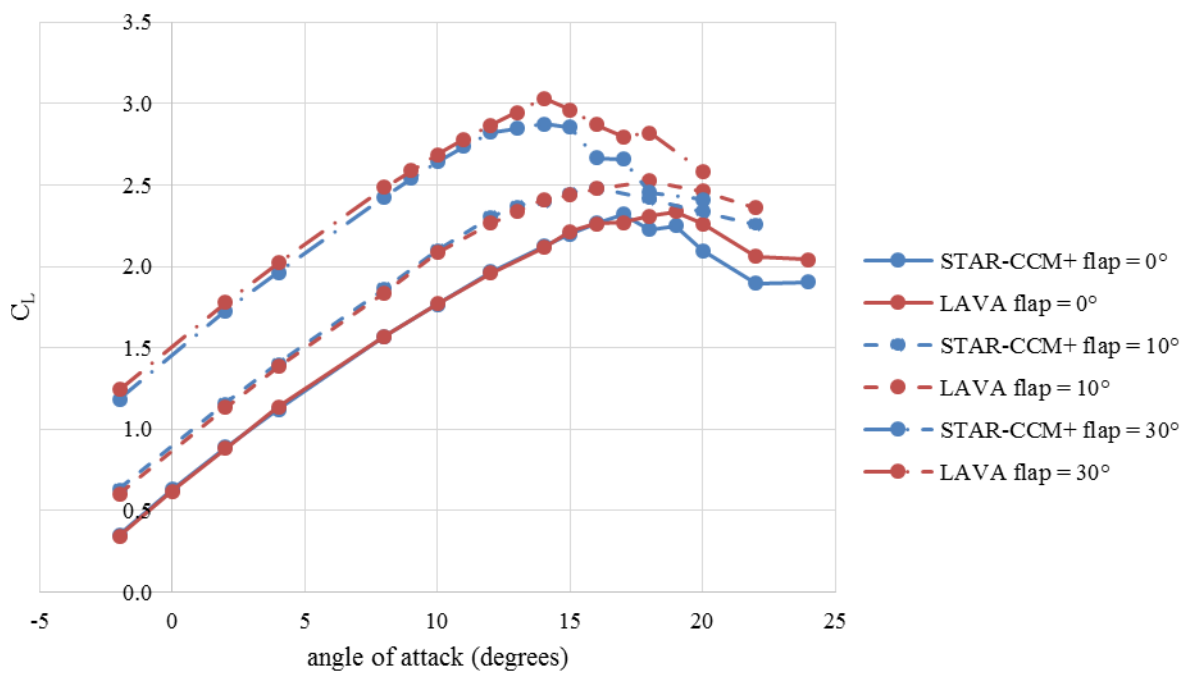

Fig. 5. Angle-of-attack sweep: C_L versus angle of attack for 0°, 10°, and 30° flap-deflection angles.

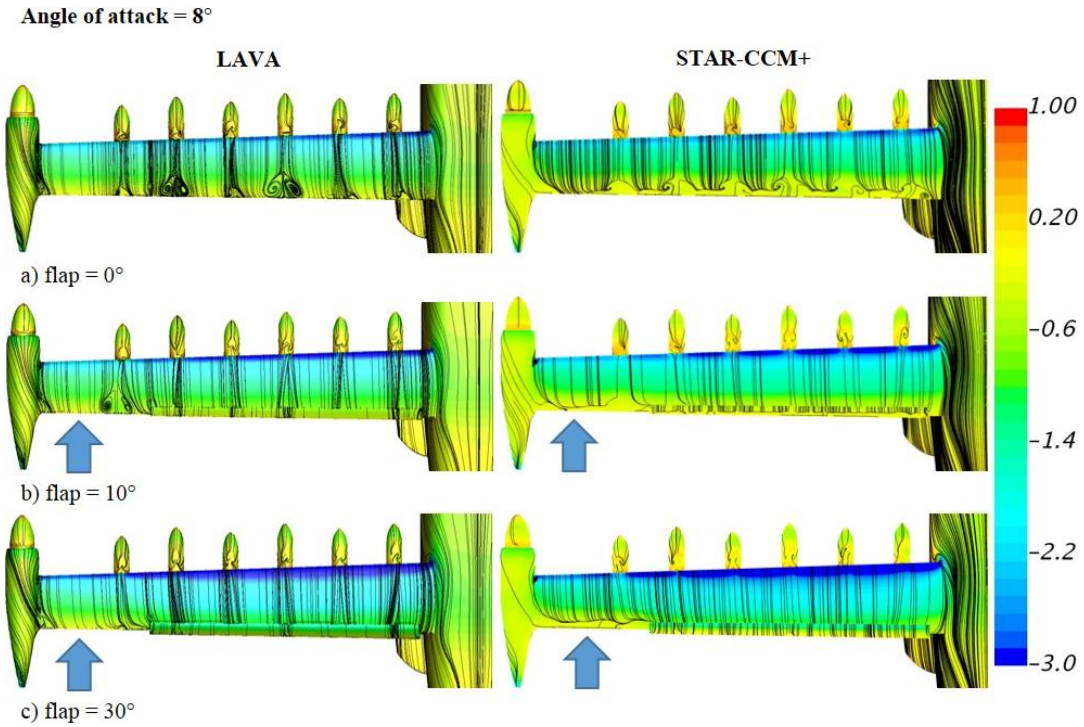

Fig. 6. Surface pressure coefficient contour of the upper surface of the wing at 8° angle of attack: a) flap = 0°; b) flap = 10°; and c) flap = 30°.

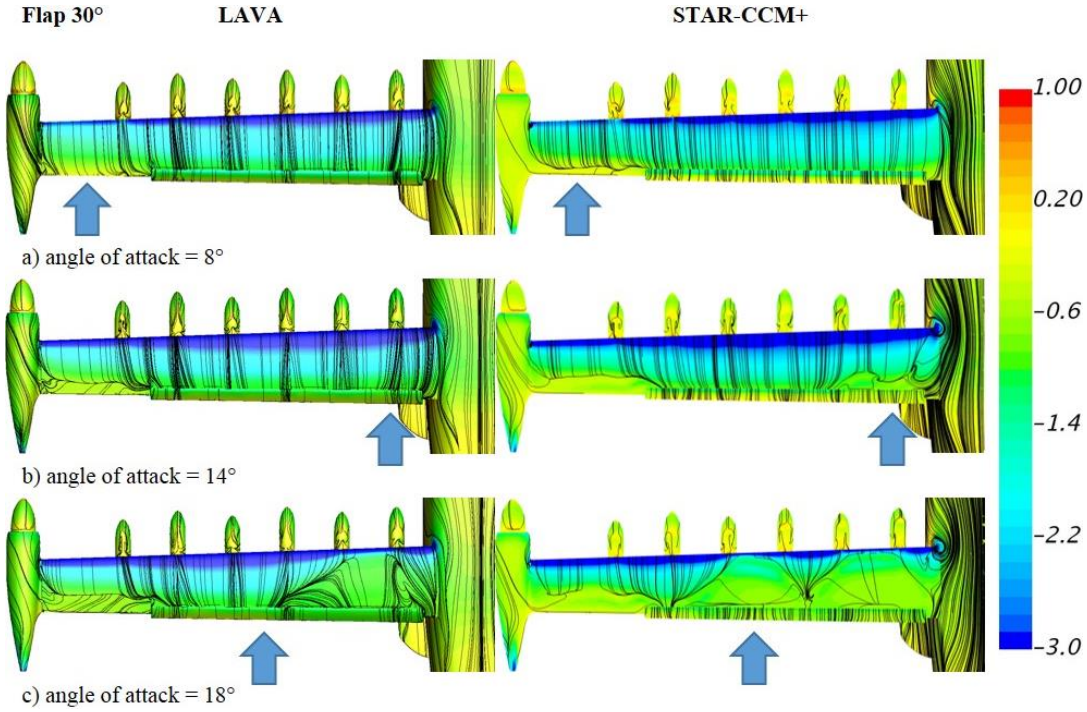

Fig. 7. Surface pressure coefficient contour of the upper surface of the wing at 30° flap deflection at selected angles of attack: a) angle of attack = 8°; b) angle of attack = 14°; and c) angle of attack = 18°.

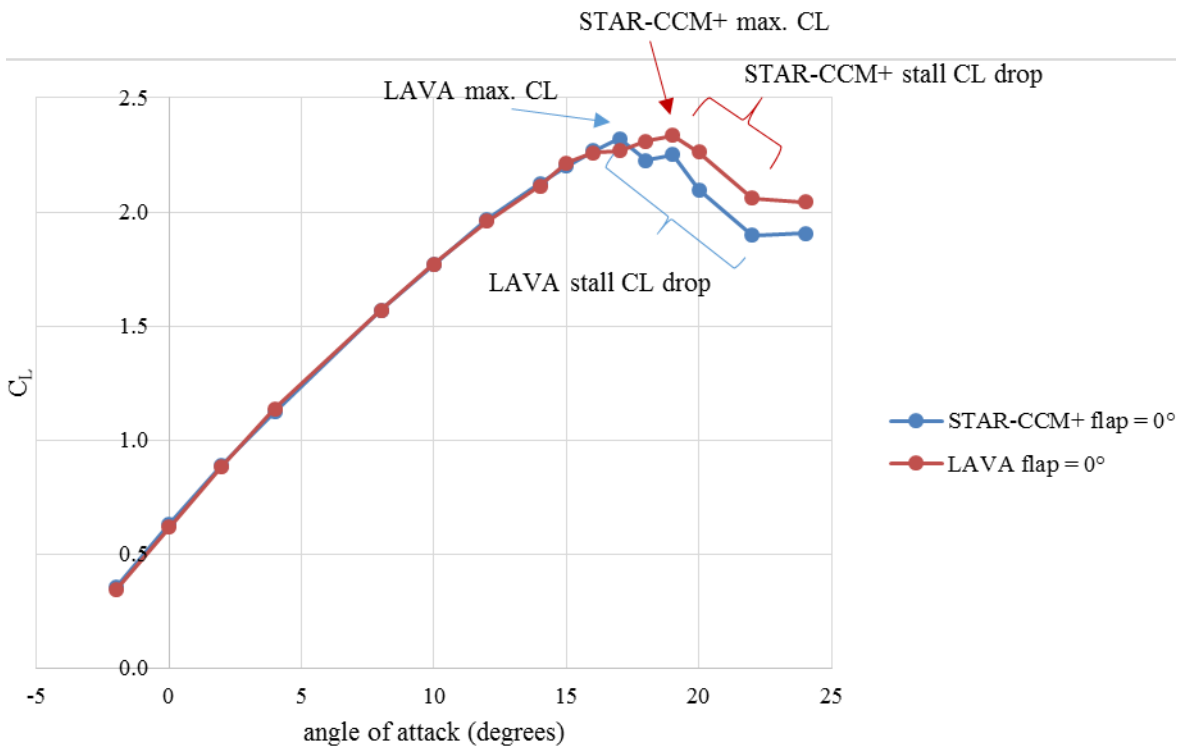

Fig. 8. Angle-of-attack sweep: C_L versus angle of attack for 0° flap-deflection angles; maximum C_L and stall for STAR-CCM+ and LAVA denoted.

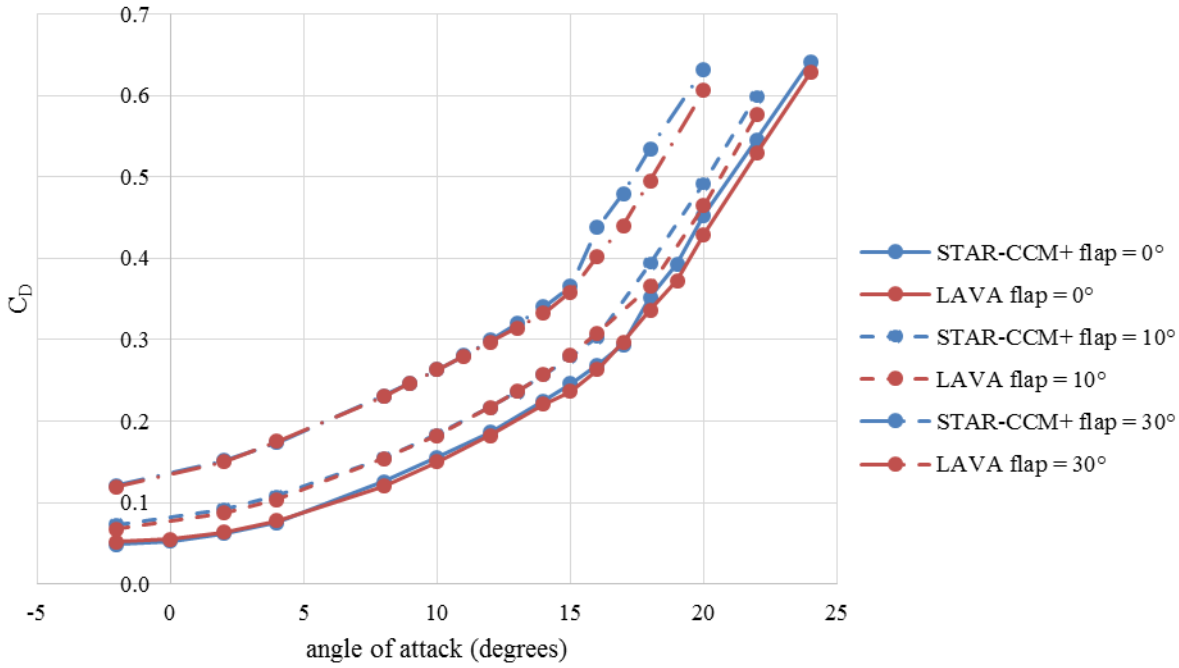

Fig. 9. Angle-of-attack sweep: C_D versus angle of attack for 0°, 10°, and 30° flap-deflection angles.

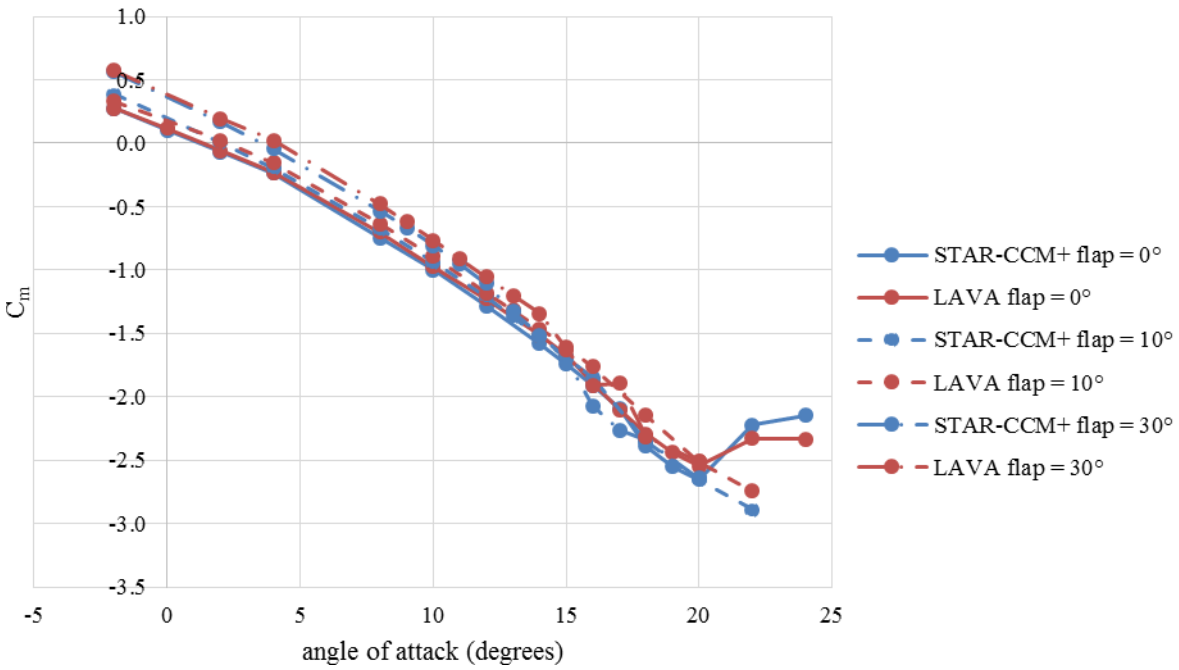

Fig. 10. Angle-of-attack sweep: C_m versus angle of attack for 0°, 10°, and 30° flap-deflection angles.

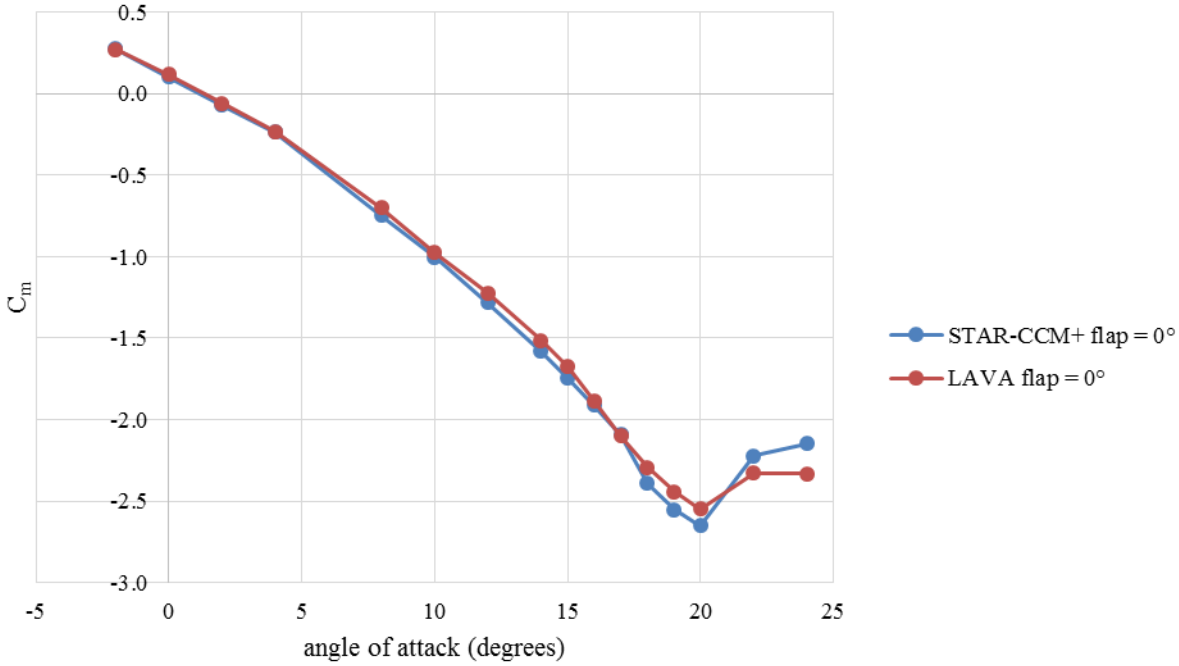

Fig. 11. Angle-of-attack sweep: C_m versus angle of attack for 0° flap-deflection angles.

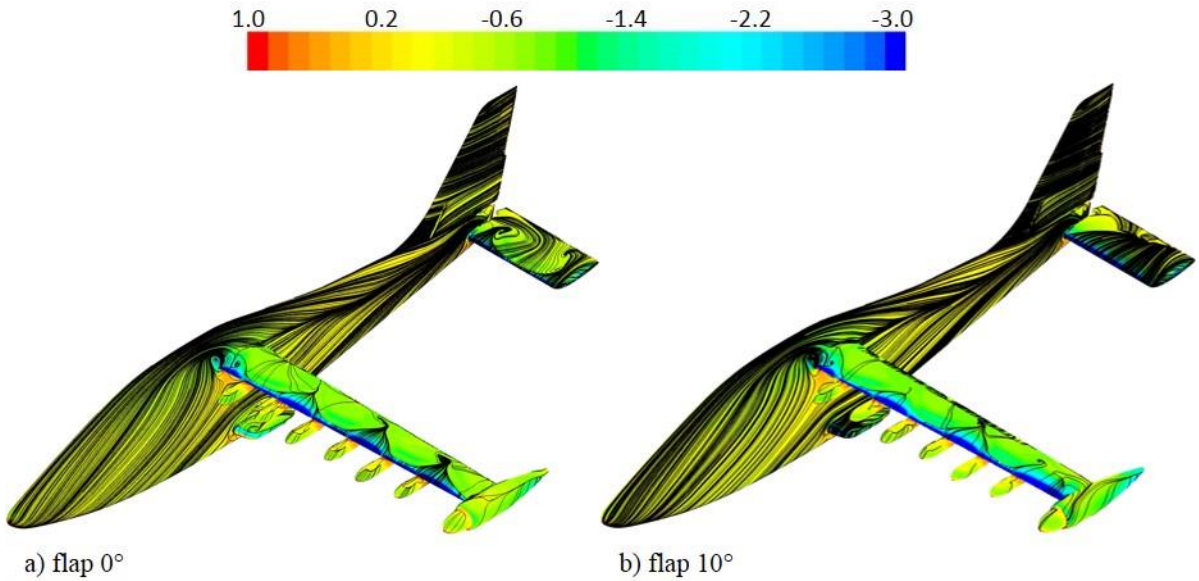

Fig. 12. STARCCM+ surface pressure coefficient contour at 22° angle of attack for simulated flap-deflection angles: a) flap = 0°; and b) flap = 10°.

C. Sideslip-Angle Sweep

Results of the sideslip-angle sweeps at a constant angle of attack of 2° are presented for 0°, 10°, and 30° flap deflections: C_L in Fig. 13, C_D in Fig. 14, C_Y in Fig. 15, C_l in Fig. 16, C_m in Fig. 17, and C_n in Fig. 18. The sideslip angles simulated are tabulated in Table 5. It should be noted that not all sideslip angles were simulated by LAVA; LAVA simulated 5° and 20° while STAR-CCM+ simulated 5°, 10°, 15°, and 20°. As with the angle-of-attack sweep study, control surfaces other than the flap were set to the neutral position (no deflection). The atmospheric conditions for each flap deflection are tabulated in Table 4.

Comparing the presented force and moment coefficients of STAR-CCM+ and LAVA, results from the two solvers are in agreement in both values and trends. The C_L, shown in Fig. 13, is approximately constant from 0° to 5° sideslip angle, then decreases as sideslip angle increases for the simulated flap deflections. The C_D, shown in Fig. 14, decreases as the sideslip angle increases. The slope of C_D as a function of sideslip angle is identical for 0°, 10°, and 30° flap deflections. Similarly, the C_Y, shown in Fig. 15, decreases linearly with increase in sideslip angle with flap deflection having negligible effect. The C_l, Fig. 16, decreases linearly with increase in sideslip angle, however, the rate of change decreases with increase with flap-deflection angle. The C_m, Fig. 17, is approximately constant from 0° to 15° sideslip angle, and then suddenly the C_m increases at 20° sideslip angle for all flap deflections. This trend is only shown in STAR-CCM+ result (LAVA did not run 10° and 15° sideslip angle). The C_m at 5° and 20° sideslip angle, however, compare well between STAR-CCM+ and LAVA.

The increase in pitching moment for sideslip angle above 20° can be analyzed by examining Fig. 19. Figure 19 shows the surface pressure coefficient contour of the upper surface of the stabilator for 0° flap deflection at 5°, 10°, 15°, and 20° sideslip angles with constant angle of attack of 2°. The surface pressure coefficient on the upper surface fo the stabilator for sideslip angles of 5° to 15° remains approximately constant. At 20°, however, there is increase in surface pressure on the upper surface of the stabilator, denoted by a blue arrow in the figure. This increase in the surface pressure decreases the lift generated by the stabilator, effectively increasing the C_m, as seen in Fig. 17.

The surface pressure coefficient contour of 0°, 10°, and 30° flap deflections at 2° angle of attack and 20° sideslip angle are presented in Fig. 20. The figure shows that there is a flow separation on the leading edge of the rudder for the simulated flap deflections. The size of the separation region is independent of the flap-deflection angle. The location of the separation regions are denoted in the figure by red arrows. There is also flow separation on the leading edge of the right wing root section for the simulated flap deflections. The size of the separation region grows in the spanwise direction with increase in the flap-deflection angle. The separation regions are denoted by blue arrows in the figure.

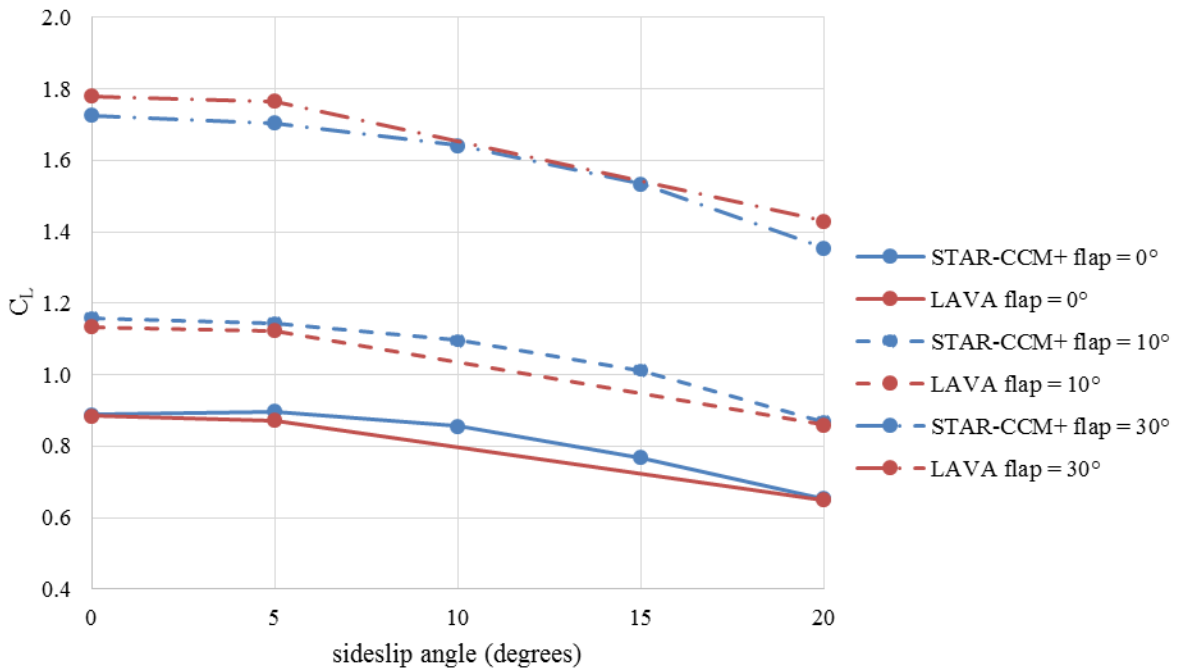

Fig. 13. Sideslip-angle sweep at 2° angle of attack: C_L versus sideslip angle for 0°, 10°, and 30° flap-deflection angles.

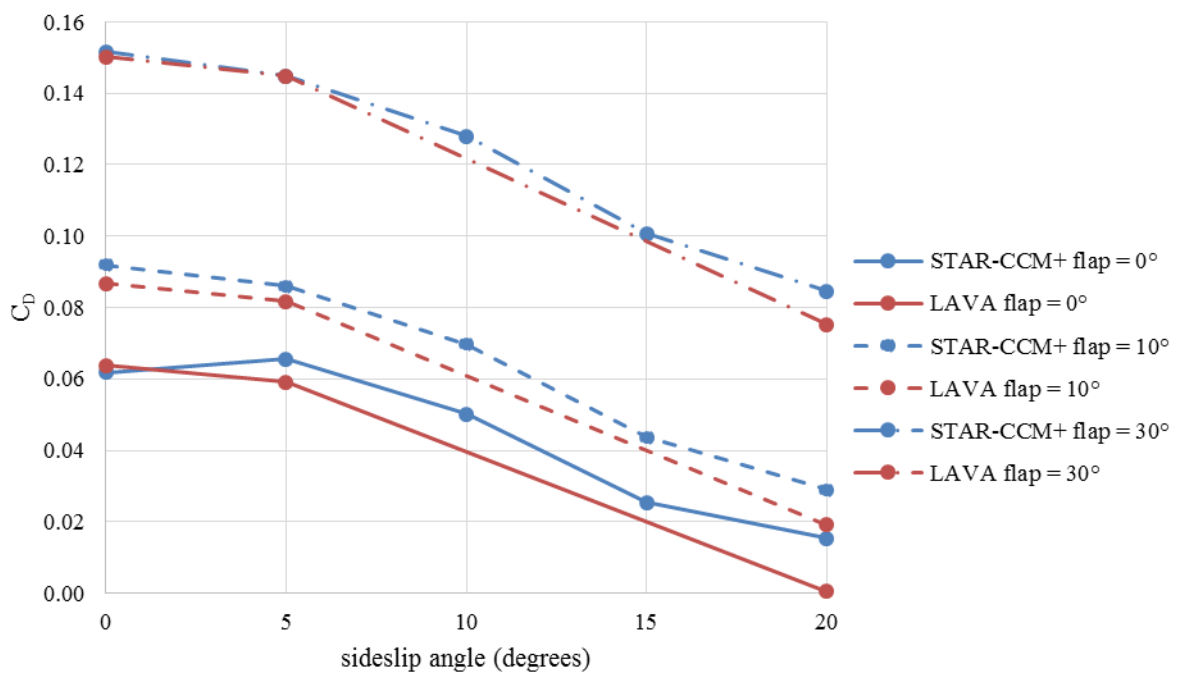

Fig. 14. Sideslip-angle sweep at 2° angle of attack: C_D versus sideslip angle for 0°, 10°, and 30° flap-deflection angles.

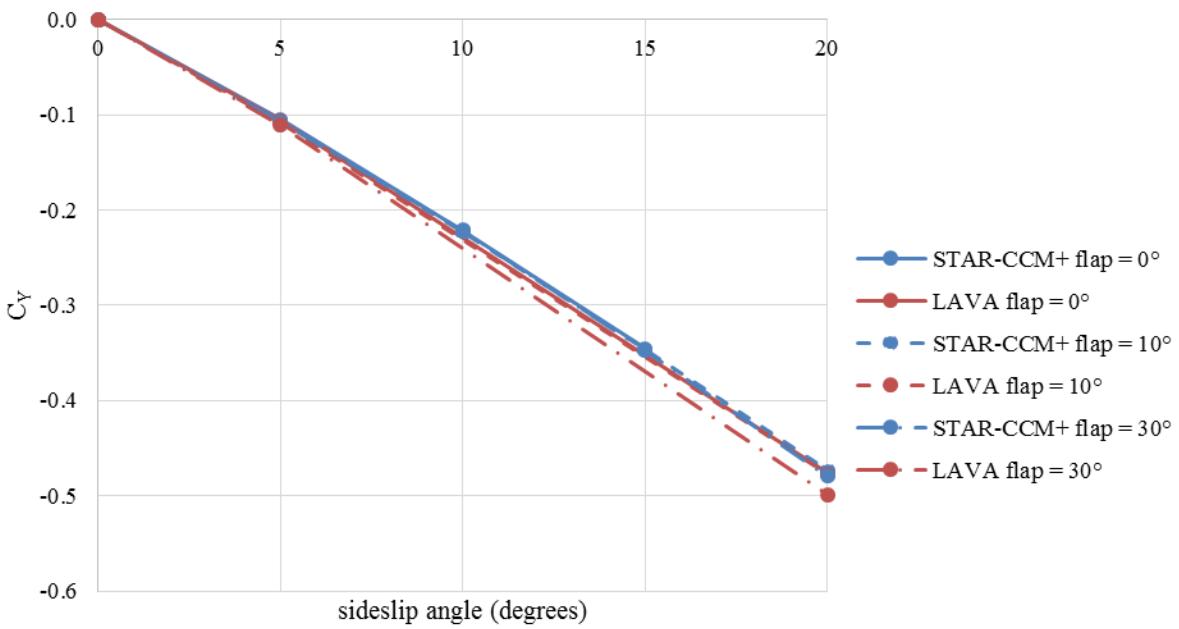

Fig. 15. Sideslip-angle sweep at 2° angle of attack: C_Y versus sideslip angle for 0°, 10°, and 30° flap-deflection angles.

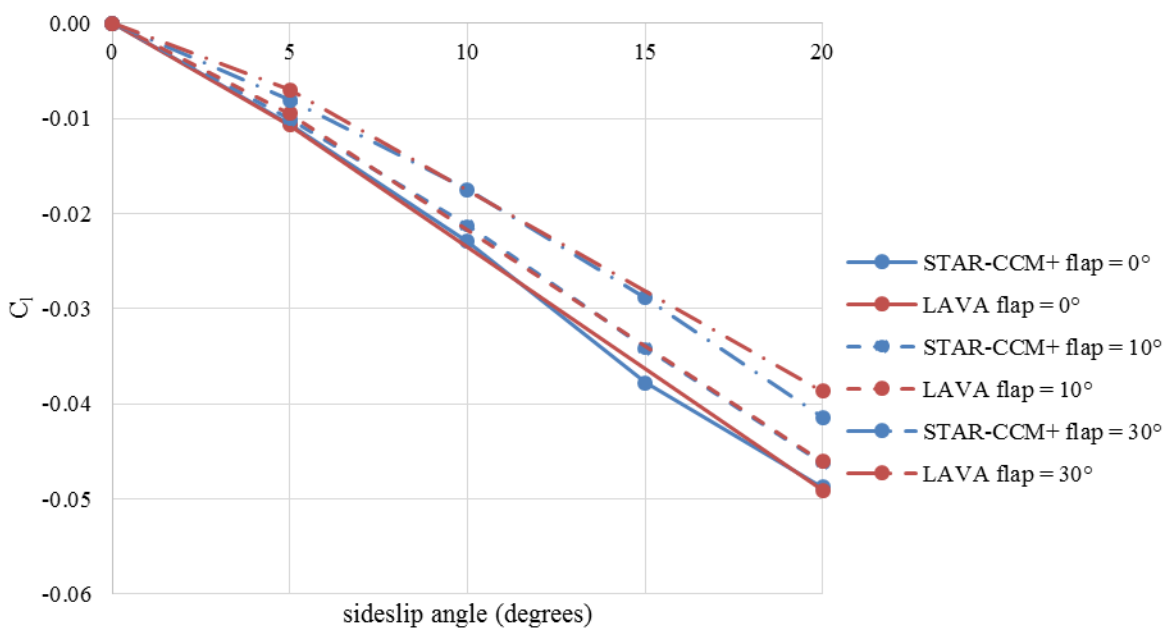

Fig. 16. Sideslip-angle sweep at 2° angle of attack: C_l versus sideslip angle for 0°, 10°, and 30° flap-deflection angles.

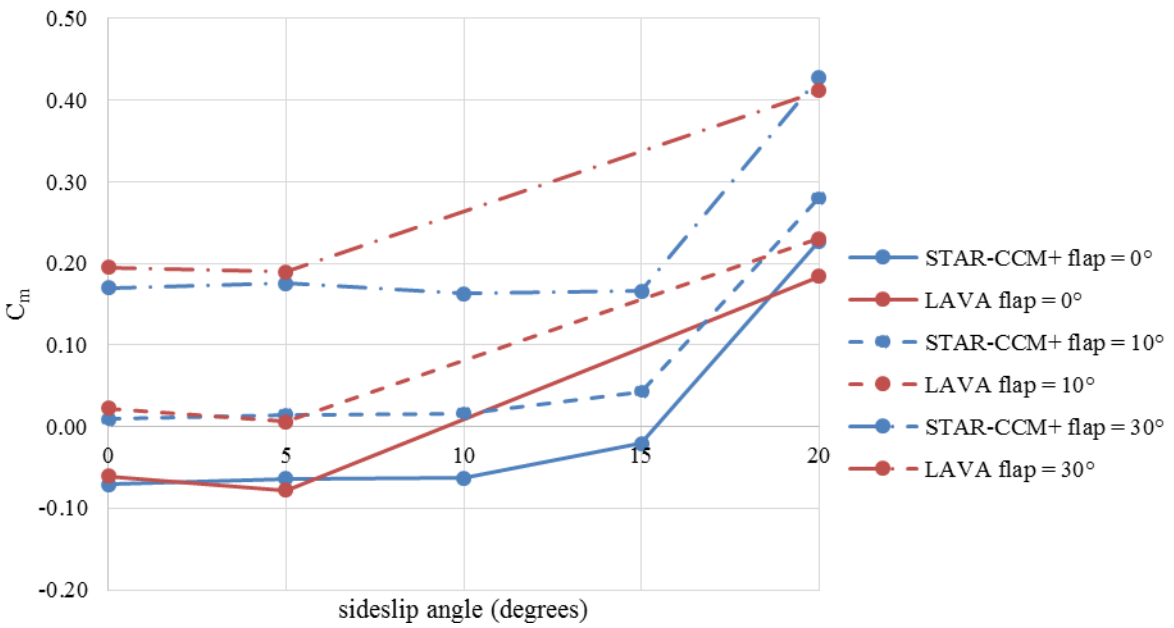

Fig. 17. Sideslip-angle sweep at 2° angle of attack: C_m versus sideslip angle for 0°, 10°, and 30° flap-deflection angles.

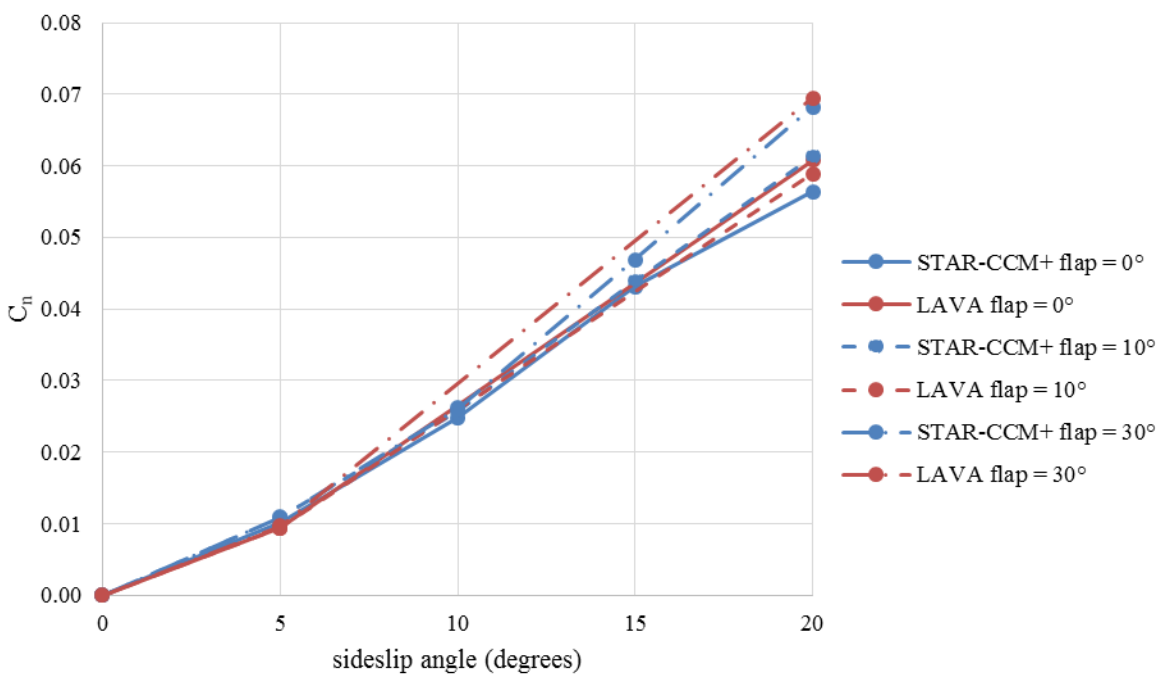

Fig. 18. Sideslip-angle sweep at 2° angle of attack: C_n versus sideslip angle for 0°, 10°, and 30° flap-deflection angles.

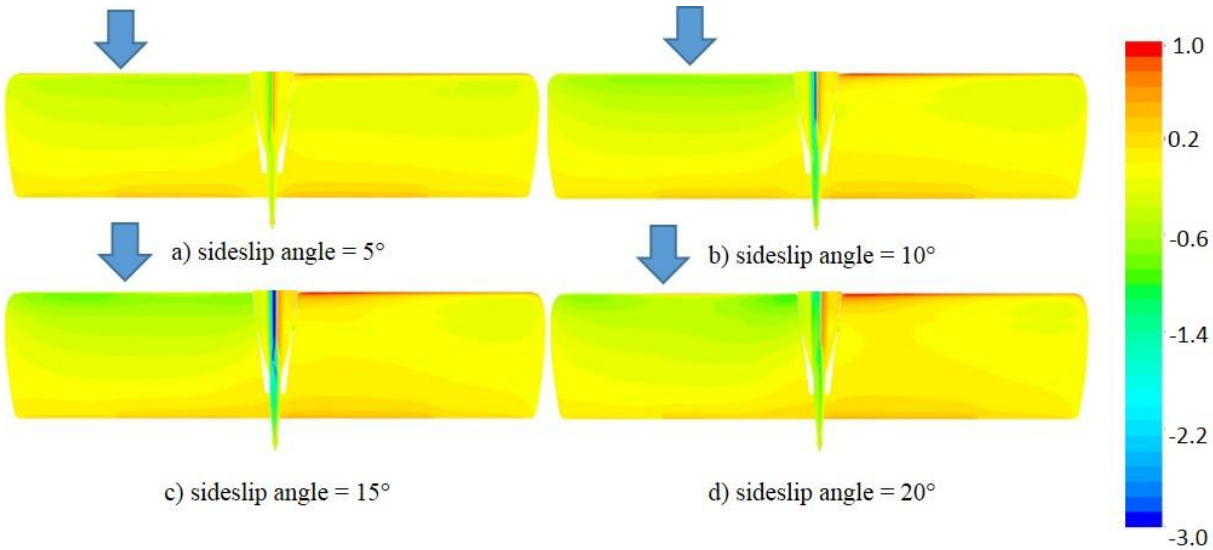

Fig. 19. STARCCM+ surface pressure coefficient contour of stabilator: 0° flap-deflection, 2° angle of attack: a) sideslip angle = 5°; b) sideslip angle = 10°; c) sideslip angle = 15°; and d) sideslip angle = 20°.

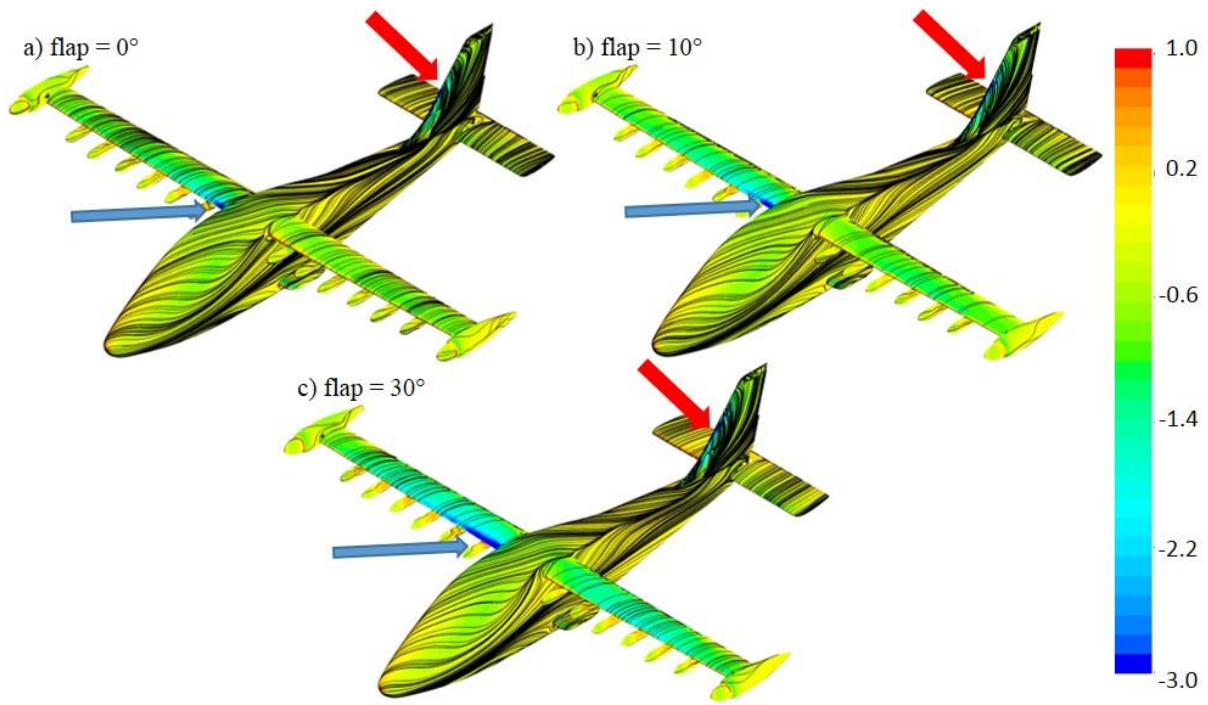

Fig. 20. STARCCM+ surface pressure coefficient contour of aircraft at 20° sideslip angle for simulated flap deflections at 2° angle of attack: a) flap = 0°; b) flap = 10°; and c) flap = 30°.

VI. Conclusion

This paper presented computational analysis of the unpowered, Mod-III of the X-57 using the STAR-CCM+ and the Launch Ascent Vehicle Aerodynamics (LAVA) flow solvers. A grid refinement study showed that adequate grid resolution was used in the simulations, with force and moment coefficients predictions being within 3 percent except for rolling moment coefficient (a small value for both flow solvers). Based on the grid resolution selected, angle-of-attack sweeps and sideslip-angle sweeps were performed.

Results of the angle-of-attack sweeps were presented with the results showing agreement between the two flow solvers. The discrepancies between the two solvers grow with increase in flap deflection due to STAR-CCM+ having outboard trailing edge separation that is not present in the LAVA solutions. The difference between the solutions of two solvers are present at angle of attack near stall due to the different separation behaviors predicted by the solvers - STAR-CCM+ does not use quadratic constitutive relationship with the turbulence model. Results also show that flap deflections do not change the lift curve slope in the linear region; however, increasing the flap-deflection angle increases the maximum lift while lowering the angle of attack at which the lift occurs. Additionally, a sharp increase in pitching moment was observed at 0° flap deflection due to flow separation on the upper surface of the stabilator that did not occur at higher flap-deflection angles.

Sideslip-angle sweep results showed that forces and moments change linearly with change in sideslip angle except for the pitching moment. Investigation of the flow over the stabilator showed that while surface pressure is approximately constant from 5° to 15° sideslip angle, it increases at 20° sideslip angle, decreasing the lift generated by the stabilator and producing a sharp increase in the pitching moment. The surface pressure coefficient also showed a separation region on the leading edge of the wing, near the wing-fuselage junction, that grows in spanwise direction with an increase in flap-deflection angle.

References

[1] Siemens, "Simcenter Star-CCM+," 2019. https://mdx.plm.automation.siemens.com/star-ccm-plus [retrieved 1 May 2019].

[2] Kiris, C. C., Housman, J. A., Barad, M. F., Brehm, C., Sozer, E., and Moni-Yeta, S., "Computational Framework for Launch, Ascent, and Vehicle Aerodynamics (LAVA)," *Aerospace Science and Technology,* Vol. 55, August 2016, pp. 189-219. doi: 10.1016/j.ast.2016.05.008

[3] Duensing, J. C., Yoo, S. Y., Maldonado, D., Housman, J. A., Jensen, J. C., and Kiris, C. C., "Establishing Best Practices for X-57 Maxwell CFD Database Generation," AIAA-2019-0274, January 2019. doi: 10.2514/6.2019-0274

[4] Venkatakrishnan, V., "On the Accuracy of Limiters and Convergence to Steady State solutions," AIAA-93-0880, January 1993. doi: 10.2514/6.1993-880

[5] Spalart, P. R., and Allmaras, S. R., "A One-Equation Turbulence Model for Aerodynamic Flows," AIAA-92-0439, January 1992. doi: 10.2514/6.1992-439

[6] Yamamoto, K., Tanaka, K., and Murayama, M., "Effect of a Nonlinear Constitutive Relation for Turbulence Modeling on Predicting Flow Separation at Wing-Body Juncture of Transonic Commercial Aircraft," AIAA-2012-2895, June 2012. doi: 10.2514/6.2012-2895

[7] Anonymous, "3rd AIAA CFD High Lift Prediction Workshop Gridding Guidelines," https://hiliftpw.larc.nasa.gov/Workshop3/GriddingGuidelines-HiLiftPW3-v10.pdf, June 2016 [retrieved 1 May 2019].

[8] BETA-CAE, ANSA pre-processing tool website, www.beta-cae.com/ansa.htm [retrieved 1 May 2019].

[9] Pointwise, "Software and Services for CFD Mesh Generation," 2019. http://www.pointwise.com/products/index.html [retrieved 1 May 2019].

[10] Chan, W. M., Pandya, S. A., Rogers, S. A., Jensen, J. C., Lee, H. C., Kao, D. L., Buning, P. G., Meakin, R. L., Boger, D. A., and Nash, S. M., "Chimera Grid Tools User's Manual, Version 2.2" http://people.nas.nasa.gov/~wchan/cgt/doc/man.html, June 2018 [retrieved 1 May 2019].

[11] Bui, T. T., "Analysis of Low-Speed Stall Aerodynamics of a Swept Wing with Seamless Flaps," AIAA-2016-3720, June 2016. doi: 10.2514/6.2016-3720